# LANGMUIR

Combined Experimental and Theoretical Study of the Structure of AuPt Nanoparticles Prepared by Galvanic Exchange

Aliya S. Lapp,[†,‡,∥] Zhiyao Duan,[†,§,∥] Graeme Henkelman,*,[†,§] and Richard M. Crooks*,[†,‡]

†Department of Chemistry, ‡Texas Materials Institute, and §Oden Institute for Computational and Engineering Sciences, The University of Texas at Austin, 2506 Speedway, Stop A5300, Austin, Texas 78712-1224, United States

Ⓢ *Supporting Information*

ABSTRACT: In this article, experiment and theory are combined to analyze Pb and Cu underpotential deposition (UPD) on ∼1.7 nm Au nanoparticles (NPs) and the AuPt structures that result after galvanic exchange (GE) of the UPD layer for Pt. Experimental Pb (0.49 ML) and Pt (0.50 ML) coverages are close to values predicted by density functional theory-molecular dynamics (DFT-MD, 0.59 ML). DFT-MD reveals that the AuNPs spontaneously reconstruct from cuboctahedral to a (111)-like structure prior to UPD. In the case of Pb, this results in the random electrodeposition of Pb onto the Au surface. This mechanism is a consequence of opposing trends in Pb−Pb and Pb−Au coordination numbers as a function of Pb coverage. Cu UPD is more complex, and agreement between theory and experiment takes into account

ligand effects (e.g., SO_4^{2-} present as the electrolyte) and the electric double layer. Importantly, AuPt structures formed upon Pt GE are found to differ markedly depending on the UPD metal. Specifically, cyclic voltammetry indicates that the Pt coverage is ∼0.20 ML greater for Cu UPD/Pt GE (0.70 ML) than for Pb UPD/Pt GE (0.50 ML). This difference is corroborated by DFT-MD theoretical predictions. Finally, DFT-MD calculations predict the formation of surface alloy and core@shell structures for Pb UPD/Pt GE and Cu UPD/Pt GE, respectively.
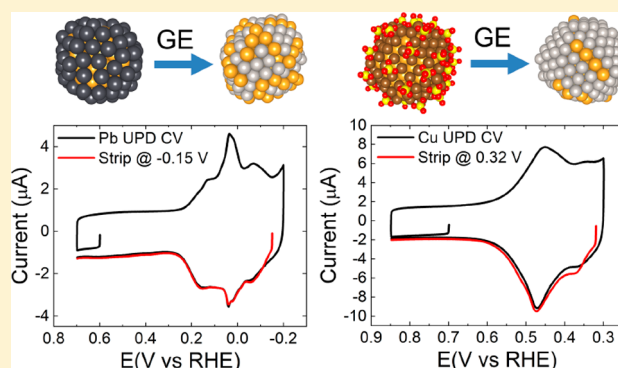
INTRODUCTION

Nanoparticle (NP) catalysts consisting of a single-metal or multimetal alloy core capped with a single-atom-thick partial or full shell are important for many different chemical and electrochemical reactions.[1−3] For example, they minimize the use of expensive, catalytically active metals by maximizing the number of active surface atoms.[3] Additionally, core@shell structuring enables fine-tuning of the catalytically active shell by exerting control over the size, shape, composition, and ordering of the core.[4−7] Many interesting catalytic effects of these types of materials are observed, particularly when the size of the NPs is ≲3 nm.[6−11]

One popular method for preparing these types of materials involves electrochemical underpotential deposition (UPD) of the shell metal onto the core, followed by galvanic exchange (GE) of the shell for a second metal.[1,2,5,12−17] UPD is a process by which a single metallic monolayer (ML) is deposited onto a substrate at a potential positive of bulk metal deposition.[18] GE occurs when ions of a more noble metal spontaneously replace a UPD ML with a ML of the more noble metal. For example, Au@Pt NPs active for the oxygen reduction reaction (ORR),[15] methanol oxidation reaction,[17] and formic acid oxidation (FAO)[19] have been synthesized using the UPD/GE process.[15,20] Because of their small size and complex structures, however, the characterization of core@

shell NPs is often incomplete. This, in turn, makes it difficult to draw structure−function correlations. For example, we recently showed that bimetallic AuPt NPs prepared by a direct Pt ML deposition technique, known as the hydride-termination method,[13,21,22] yield alloys[23] rather than the core@shell structure anticipated by extrapolation from macroscale materials.[21]

There is an extensive body of literature focused on Cu and Pb UPD on macroscale Au substrates.[18,20,24−27] Despite the widespread use of UPD/GE for synthesizing NPs, however, the understanding of UPD processes on NPs,[14,28−33] particularly those in the <3 nm size range, is less well developed. The theoretical examination of UPD on NPs, in particular, has been limited in both number and depth.[16,29−31,34,35] Dendrimer-encapsulated NPs (DENs), which we[6,11,36−38] and others[39−41] have previously reported, are well suited for combining experimental and theoretical studies because of their small (1 to 2 nm) and nearly monodisperse sizes and compositions.[6] These factors minimize computational costs, avoid the theoretical limitations of treating heterogeneity, and eliminate

uncertainties associated with calculations that consider only slabs of larger NPs.

Cu UPD[15,29,30,42−44] and Pb UPD[16,19] have previously been studied on DEN cores. Cu UPD on Au DENs was first used as a precursor for preparing Au@Pt NPs.[15] However, direct immobilization of the DENs onto glassy carbon electrodes precluded complete structural characterization.

In addition to preparing Au@Pt DENs using a Cu UPD intermediate, we also reported their synthesis via Pb UPD.[16] This approach yielded considerably lower surface Pt coverage (55−57% of a full Pt ML) relative to Cu UPD/Pt GE,[15] but it still resulted in the formation of electrocatalysts active for the ORR[16] and FAO.[19] Moreover, density functional calculations indicated that Pt(100) sites initially present on the surface of the cuboctahedral Au@Pt DENs undergo a rapid conversion to Pt(111).[16] This structural change was found to positively impact the electrocatalytic activity of these materials for the FAO reaction relative to Pt-only and Au-only DENs.[19]

On the basis of our earlier study,[23] which clearly demonstrated the pitfalls of extrapolating structural motifs determined for macroscale materials to the nanoscale, we now investigate an even more interesting question. Specifically, do AuPt NPs prepared by slightly different methods have the same or different structures, and if the latter, why? The answer to this question could have a significant impact on our understanding of electrocatalysis, particularly for reactions sensitive to ensemble effects (e.g., FAO)[45,46] or for reactions where both Pt and Au are catalytically active (e.g., CO oxidation in alkaline media).[43,47] To address this question, we deposited either Cu or Pb UPD MLs onto well-defined, ∼1.7 nm Au cores and then exchanged the UPD metal for Pt. Detailed characterization reveals that the choice of the UPD metal strongly impacts the final structures of the resulting bimetallic NPs. Companion results from a first-principles density functional theory (DFT) study provide insights into the underlying reasons for these findings.

■ EXPERIMENTAL SECTION

Chemicals and Materials. A 9.0 wt % solution of amine-terminated, sixth-generation poly(amidoamine) (PAMAM) dendrimers (G6-NH$_2$) in methanol was obtained from Dendritech, Inc. (Midland, MI). The methanol was evaporated and the dendrimers were reconstituted in sufficient water to yield a 0.10 mM G6-NH$_2$ stock solution. A 0.50 M NaOH solution, NaBH$_4$ (99.9%), HAuCl$_4$ (≥99.9%), Pb(NO$_3$)$_2$ (99.9%), and HPLC grade 2-propanol (99.9%) were purchased from Sigma-Aldrich. K$_2$PtCl$_4$ (99.9%), CuSO$_4$ (98%, anhydrous), and 70% HClO$_4$ (in H$_2$O) were obtained from Fisher (New Jersey). All solutions were prepared using deionized (DI) Milli-Q water (18.2 MΩ·cm; Millipore, Bedford, MA).

TEM grids were purchased from EM Sciences (Gibbstown, NJ, catalog numbers CF400-Cu-UL and LC400-Cu-UL). Vulcan carbon (EC-72R) was purchased from ElectroChem, Inc. (Woburn, MA). The working (glassy carbon, 3.0 mm), reference (Hg/Hg$_2$SO$_4$), and counter (glassy carbon rod) electrodes were purchased from CH Instruments (Austin, TX).

Synthesis of Au DENs. The synthesis of Au DENs (denoted as G6-NH$_2$(Au$_{147}$), where 147 reflects the AuCl$_4^-$/G6-NH$_2$ ratio in the precursor solution) has been reported previously and shown to result in nearly size-monodisperse AuNPs.[23,48] Briefly, a 2.0 μM aqueous G6-NH$_2$ dendrimer solution was prepared by adding 0.20 mL of a 0.10 mM stock to 8.65 mL of water. AuCl$_4^-$ was encapsulated within the dendrimers by the dropwise addition of HAuCl$_4$ (0.147 mL of a 20.0 mM stock solution) with vigorous stirring. Within 2 min, the encapsulated AuCl$_4^-$ was chemically reduced with a solution consisting of 1.0 mL of 0.30 M NaOH and an 11- to 12-fold molar

excess of NaBH$_4$. For this step, NaOH was added to the NaBH$_4$ (in a weighing boat) immediately before transfer. Upon reduction, the solution changed color from light yellow to brown. Deactivation of the residual BH$_4^-$ by air was allowed to proceed for at least 12 h before characterizing the resulting NPs.

NP Characterization. UV−vis spectra were obtained using a Hewlett-Packard 8453 spectrometer. NP imaging was performed using a JEOL 2010F transmission electron microscope (TEM) with an operating voltage of 200 kV and a point-to-point resolution of 0.19 nm. TEM analysis of G6-NH$_2$(Au$_{147}$) was carried out by drop casting 2.0 μL of a 2.0 μM DENs solution onto a carbon-coated Cu grid and then drying in air. Grids for analyzing the AuPt DENs were prepared by swiping lacey carbon-coated Cu TEM grids across the surface of the electrodes used for electrochemical synthesis and characterization.

Cyclic Voltammetry (CV). Electrochemical synthesis and characterization were carried out using a CH Instruments 630E potentiostat in conjunction with a 3.0 mm glassy carbon working electrode (GCE), glassy carbon rod counter electrode, and Hg/Hg$_2$SO$_4$ (MSE) reference electrode. The GCEs were polished successively with 1.0, 0.3, and 0.05 μm alumina (2 min each) before use. Excess alumina was removed by sonication in Milli-Q water for ∼10−15 min. DEN inks were prepared as previously described.[23] Briefly, ∼1.0 mg of VC was dispersed into 0.20 mL of isopropanol (IPA) using sonication. After a homogeneous mixture was achieved (∼15 min), 1.0 mL of 2.0 μM G6-NH$_2$(Au$_{147}$) DENs was added and the ink was sonicated for an additional 15 min and then drop cast (6.0 μL) onto the GCE and dried under a gentle flow of N$_2$.

Electrochemical cleaning of the DENs and Au and AuPt surface-characterization CVs was carried out using a solution of N$_2$-purged 0.10 M HClO$_4$. Electrochemical cleaning was performed by scanning the electrode potential between 1.57 and 0 V for 20 cycles at a scan rate of 200 mV/s. The Au and AuPt surface characterization CVs were recorded using this same potential range but for only three and nine cycles, respectively, and at a scan rate of 100 mV/s.

Underpotential Deposition and Pt Galvanic Exchange (UPD/Pt GE). Pb UPD on the immobilized G6-NH$_2$(Au$_{147}$) DENs was performed in the following manner. First, a Pb UPD CV was recorded in N$_2$-purged 0.10 M HClO$_4$ containing 1.0 mM Pb(NO$_3$)$_2$. Specifically, the electrode potential was held at 0.60 V for 300 s and then scanned from 0.60 to 0.70 to −0.17 V at 5.0 mV/s. Pb linear sweep voltammograms (LSVs) were recorded by holding the electrode potential at −0.15 V for 300 s and then scanning it from −0.15 to 0.70 V at a rate of 5.0 mV/s. Cu UPD on G6-NH$_2$(Au$_{147}$) DENs was performed in N$_2$-purged 0.10 M HClO$_4$ containing 5.0 mM CuSO$_4$ using a process analogous to Pb UPD with the following differences. The electrode potential was held at 0.70 V for 300 s and was then scanned from 0.70 to 0.85 to 0.30 V at a rate of 10 mV/s. Cu LSVs were recorded by holding the electrode potential at 0.32 V for 300 s and then scanning it from 0.32 to 0.85 V at a rate of 10 mV/s.

Pt GE was used to deposit a Pt shell onto the G6-NH$_2$(Au$_{147}$) DENs. Just prior to Pt GE, the electrode potential was held at either −0.15 V (for Pb) or 0.32 V (for Cu) for 300 s. The GCE was then raised to a position slightly above the solution level, the circuit was opened, and predissolved K$_2$PtCl$_4$ (in ∼1.0 mL of 0.10 M HClO$_4$) was mixed into the cell via brief agitation with a N$_2$-purge stream. The GCE was then lowered back into solution, and the open-circuit potential (OCP) was monitored as a function of time for 400 s. The PtCl$_4^{2-}$ concentration was 2.5 mM.

Following Pt GE, the GCE was sequentially rinsed for ∼20 s in 250 mL of Milli-Q water, 5 min in 20 mL of 0.10 M HClO$_4$ (with vigorous stirring), and then briefly in 20 mL of Milli-Q water. Both the necessity and efficacy of this rinsing process were explored in depth in a previous publication[23] for a similar AuPt DEN synthesis. The as-prepared AuPt DENs (this notation is used to indicate that the structure is uncertain at this point) were then characterized by recording CVs using the same parameters as for the Au surface area CVs, with the exception that nine cycles were obtained to ensure scan reproducibility.

Density Functional Theory (DFT). Theoretical calculations were performed using DFT implemented in the Vienna ab initio simulation

package (VASP).[49,50] Core electrons were described with the projector augmented wave (PAW) method.[51,52] The Kohn−Sham wave functions for the valence electrons were expanded in a plane-wave basis set with an energy cutoff of 300 eV. The exchange-correlation energy was treated within the generalized gradient approximation. Specifically, PBEsol[53] was used, which is a modified form of the Perdew−Burke−Ernzerhof (PBE) functional designed to improve lattice parameters and surface energies in solids. A single Γ point was sufficient for integration of the Brillouin zone as a result of the finite nature of the NPs.

Density Functional Theory Molecular Dynamics (DFT-MD). DFT-MD simulations were employed to equilibrate the structures of Pb adsorption, Cu adsorption, and Cu/SO_4 adsorption on AuNPs. A time step of 1.5 fs was used, and a total time of 30 ps was carried out for each MD simulation. The temperature was held at 300 K by drawing the velocities of all atoms from a Boltzmann distribution every 10 steps.

Double Reference Method. The double reference method[54] was used to simulate the electric double layer (EDL) and determine the equilibrium potential of Cu UPD on the Au(111) surface under constant-potential conditions. Our approach is different from the original implementation of the double reference method,[54] where explicit water molecules are used to model the metal/aqueous interface. Here, the aqueous environment is treated by the continuum solvation model developed by Hennig and co-workers as implemented in the VASPsol code.[55] The relative permittivity of the solvent was set to $\epsilon_{solv} = 80$ to account for the presence of the aqueous electrolyte. This value corresponds to the permittivity of bulk water.

Details of the double reference method can be found elsewhere.[56,57] Briefly, the electric potential of the simulated electrochemical interface is varied by changing the number of electrons in the system. To maintain charge neutrality of the supercell, a uniform background of compensating counter charge was added. The charged slab, together with the compensating background charge, polarizes the electrolyte near the metal/solution interface, thereby creating an electrostatic potential profile that simulates the EDL.

For each electrochemical interface, DFT calculations were performed at various charges by inserting or deleting electrons from the simulated system. The total free energy at each point was then fit to a quadratic equation to provide a continuous free energy as a function of potential. The quadratic form is consistent with a capacitor created by the charged-slab/background-charge system, which takes the form of eq 1.
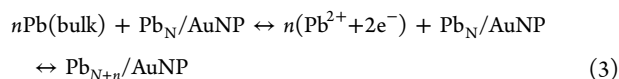
$$E(U) = -\frac{1}{2}C(U - U_{pzc})^2 + E_0 \tag{1}$$

Here, U_{pzc} refers to the potential of zero charge (PZC), E_0 is the energy at the PZC, and C is the capacitance of the metal/aqueous interface. From the quadratic equations fit to the bare slab and adsorption models, the binding energies as a function of electric potential are readily calculated.

Simulation of CVs. CVs of the UPD processes were simulated according to a method from the literature.[58] The current ($i(t)$) produced by the UPD processes can be calculated as shown in eq 2.

$$i(t) = \pm KQ_{tot}\frac{d\theta}{dU} \tag{2}$$

Here, K is the sweep rate and Q_{tot} is the total charge that the surface of AuNPs can accommodate. $\frac{d\theta}{dU}$ is the inverse of $\frac{dU}{d\theta}$, which is the differential equilibrium potential of the UPD processes with respect to the surface coverage of the deposited species (Pb or Cu atoms) in this study. To calculate the equilibrium potentials of the UPD processes, we considered the hypothetical reaction route shown in eq 3, using Pb^{2+} deposition on AuNPs as an example.

$$n\text{Pb(bulk)} + \text{Pb}_N/\text{AuNP} \leftrightarrow n(\text{Pb}^{2+}+2e^-) + \text{Pb}_N/\text{AuNP}$$
$$\leftrightarrow \text{Pb}_{N+n}/\text{AuNP} \tag{3}$$

Here, Pb in its bulk form is dissolved and then the dissolved Pb^{2+} deposits onto the AuNP. The latter reaction is the process we are interested in, and the average free-energy change of this step is ΔG^{dep} = $(G_{\text{Pb}_{N+n}/\text{AuNP}} - n\mu_{\text{Pb}^{2+}} - G_{\text{Pb}_N/\text{AuNP}} + 2neU)/n$, where $G_{\text{Pb}_N/\text{AuNP}}$ is the free energy of an AuNP coated with N Pb atoms, n is the number of Pb atoms deposited, $\mu_{\text{Pb}^{2+}}$ is the chemical potential of Pb^{2+}, and U is the applied potential. The value of $\mu_{\text{Pb}^{2+}}$ can be calculated from the standard reduction potential of Pb metal ($U^0 \equiv -0.13$ V) and the concentration of Pb^{2+} ($c_{\text{Pb}^{2+}}$) using eq 4.

$$\Delta G^{dep} = (G_{\text{Pb}_{N+n}/\text{AuNP}} - n\mu_{\text{Pb,bulk}} - G_{\text{Pb}_N/\text{AuNP}} + 2ne(U - U^0)$$
$$- nk_BT \log c_{\text{Pb}^{2+}})/n \tag{4}$$

If the vibrational entropy contributions to the free energy of solid materials are omitted and the free energies are replaced with total energies from DFT calculations, then the ΔG^{dep} term can be expressed as shown in eq 5.
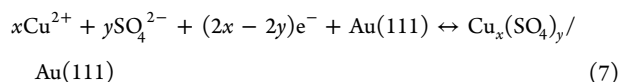
$$\Delta G^{dep} = \Delta E^{ads} - k_BT \log\left(\frac{1-\theta}{\theta}\right) + 2e(U - U^0)$$
$$- k_BT \log c_{\text{Pb}^{2+}} \tag{5}$$

Here, $\Delta E^{ads} \equiv (E_{\text{Pb}_{N+n}/\text{AuNP}} - nE_{\text{Pb, bulk}} - E_{\text{Pb}_N/\text{AuNP}})/n$ is the differential adsorption energy of Pb atoms and $k_BT \log\left(\frac{1-\theta}{\theta}\right)$ is the differential configurational entropy of the adsorbed Pb atoms with a surface coverage of θ ML. The equilibrium potential for the UPD process is then calculated as

$$U^{dep} = -\frac{\Delta G^{dep}}{2e} \tag{6}$$

Consequently, eq 6 can be inserted into eq 2 to calculate the CV current.

For the calculation of Cu/SO_4 coadsorption on AuNPs, the reaction shown in eq 7 is assumed.

$$x\text{Cu}^{2+} + y\text{SO}_4^{2-} + (2x - 2y)e^- + \text{Au(111)} \leftrightarrow \text{Cu}_x(\text{SO}_4)_y/$$
$$\text{Au(111)} \tag{7}$$

In this case, the free-energy change per deposited Cu atom is calculated as shown in eq 8.

$$\Delta G^{dep} = \Delta E^{ads} - k_BT \log\left(\frac{1-\theta}{\theta}\right) + (2x - 2y)/x(U - U^0)$$
$$- k_BT \log c_{\text{Cu}^{2+}} - y/xk_BT \log c_{\text{SO}_4^{2-}} \tag{8}$$

The calculation of ΔE^{ads} in the SO_4 coadsorption case requires the chemical potential of the solvated SO_4^{2-} ions. For this, we employed a previously reported expression.[59] When the double reference method is used to calculate the potential dependent energies, $\Delta E^{ads}(\theta)$ becomes $\Delta E^{ads}(\theta, U)$. To calculating the chemical potential of NO_3^-, we used the reduction reaction, $NO_3^-(aq) + 4H^+(aq) + 3e^- \rightarrow NO(g) + 2H_2O(l)$, which has a standard reduction potential of 0.96 V.

■ RESULTS AND DISCUSSION

Synthesis and Characterization of G6-NH₂(Au₁₄₇) DENs. The $G6\text{-}NH_2(\text{Au}_{147})$ DEN synthesis is discussed in the Experimental Section. Briefly, the DENs were prepared by combining $G6\text{-}NH_2$ dendrimers and sufficient $HAuCl_4$ to yield a 147:1 $AuCl_4^-/G6\text{-}NH_2$ ratio and then reducing the resulting composites with excess $NaBH_4$. We have previously shown that this procedure reliably yields AuNPs having narrow size distributions.[23,48]

Figure S1a shows the UV−vis spectrum of the $G6\text{-}NH_2(\text{Au}_{147})$ DEN cores. Two features are important: a small, broad plasmon band centered at ∼520 nm and a
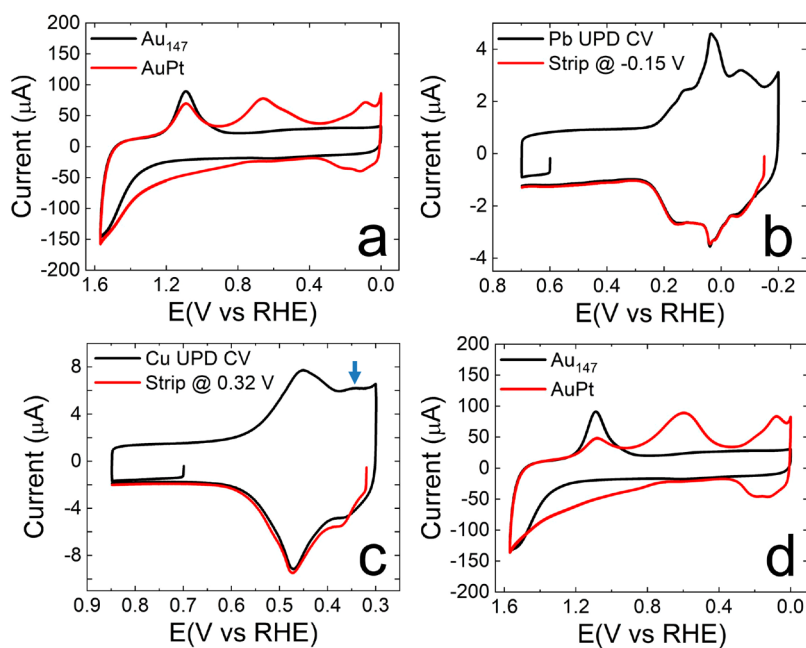
Figure 1. (a,d) Cyclic voltammograms (CVs) before (black traces) and after (red traces) Pt deposition onto G6-NH$_2$(Au$_{147}$) DENs using (a) Pb UPD/Pt GE and (d) Cu UPD/Pt GE. (b,c) CVs (black traces) corresponding to (b) Pb UPD and (c) Cu UPD on G6-NH$_2$(Au$_{147}$) DENs. The associated LSVs are shown in red. The LSVs were recorded after holding the electrode potential for 300 s at either −0.15 V (Pb) or 0.32 V (Cu). The blue arrow in (c) highlights a peak that resembles the second stage (~1.0 ML Cu) of Cu UPD onto Au(111).[18] The CVs in (a,d) were recorded in N$_2$-purged 0.10 M HClO$_4$ at a scan rate of 100 mV/s. The electrolyte in (b) and (c) was N$_2$-purged 0.10 M HClO$_4$ containing (b) 1.0 mM Pb(NO$_3$)$_2$ and (c) 5.0 mM CuSO$_4$ and the scan rates were (b) 5.0 mV/s and (c) 10.0 mV/s.

monotonic increase in absorbance toward shorter wavelengths. The combination of these features is characteristic of AuNPs having sizes of <2 nm.[16] TEM (Figure S1) confirms the spectroscopic data by revealing an average NP size of 1.7 ± 0.3 nm for the G6-NH$_2$(Au$_{147}$) DEN cores. This value is in good agreement with both the theoretical diameter of an Au$_{147}$ cuboctahedral NP (~1.6 nm)[16] and previous experimental reports.[15,16,19,23,48]

The first step in converting the Au cores to AuPt NPs involves immobilizing the G6-NH$_2$(Au$_{147}$) DENs onto Vulcan carbon (VC). The full details of this procedure are provided in the Experimental Section, but, briefly, G6-NH$_2$(Au$_{147}$) DENs were added to a premixed solution of VC in IPA and sonicated for ~15 min. This ink was then drop cast onto a GCE and dried under a gentle flow of N$_2$.

The black trace in Figure 1a is a CV of the G6-NH$_2$(Au$_{147}$) DENs prepared as described in the previous paragraph. The prominent peak at ~1.1 V corresponds to the reduction of AuO$_x$, which is formed by the potential excursion to 1.57 V. This peak can be integrated and converted to the total Au surface area (SA) using the commonly accepted charge density conversion factor of 390 μC/cm^2.[60] The resulting value is Au$_i$ = 0.28 cm^2, where subscript i represents the initial Au SA prior to UPD or GE.

Synthesis of AuPt DENs via Pb UPD/Pt GE. As discussed in the Experimental Section, UPD of Pb onto the G6-NH$_2$(Au$_{147}$) DEN cores was carried out in N$_2$-purged, 0.10 M HClO$_4$ containing 1.0 mM Pb(NO$_3$)$_2$ according to the following procedure. First, a Pb UPD CV (Figure 1b, black trace) was recorded. This CV was used to determine the end of the Pb UPD potential range for subsequent steps, which was chosen to be just positive of the onset of bulk Pb deposition at −0.15 V. Second, to ensure that no bulk deposition of Pb occurs at this potential, the electrode was held at −0.15 V for

300 s, and then an LSV was obtained by scanning in the positive direction to 0.70 V (Figure 1b, red trace). The fact that the resulting LSV overlays the Pb UPD CV confirms the absence of bulk Pb deposition. This suggests that the foregoing process coats the Au$_{147}$ cores with a single UPD ML of Pb.

Focusing now on the Pb UPD CV in Figure 1b, Pb deposition peaks are centered at 0.15, 0.04, and −0.07 V, and stripping peaks are present at 0.03 and 0.16 V. These values are in accord with our prior reports of Pb UPD on G6-NH$_2$(Au$_{147}$) DENs.[16,19] By analogy to reports of Pb deposition onto larger (~4−82 nm) AuNPs,[61−64] we previously discussed Pb UPD (and stripping) onto Au$_{147}$ DENs in terms of sequential, facet-by-facet processes.[16] For example, the two principal oxidation peaks at 0.03 and 0.16 V were assigned to Pb stripping from the Au(100) and Au(111) facets, respectively.[16] For AuNPs as small as those used here (~1.7 nm), however, a facet-by-facet mechanism is likely an oversimplification. For instance, the sharing of atoms between facets is so dominant for 147-atom cuboctahedral NPs that only a single atom is unique to a (111) facet.[29] As we will discuss later, the Pb UPD behavior on Au DENs can be successfully interpreted without invoking a facet-by-facet mechanism.

The Pb SA (0.24 cm^2) was calculated by integrating the Pb LSV in Figure 1b and then converting this value to SA using a charge density of 413 μC/cm^2.[16] Recalling that the initial Au SA was Au$_i$ = 0.28 cm^2, the Pb/Au$_i$ SA ratio is 0.86. This value is close to that which we found in a previous report (~1.1).[16] There are multiple ways of defining UPD coverage on NPs.[16,30,61] In the present report, we define 1.0 ML of Pb as the number of atoms required to construct a closed cuboctahedral shell over the NP core. For example, a 147-atom cuboctahedral NP contains 92 shell atoms. The next complete shell would contain 162 atoms, which we define as
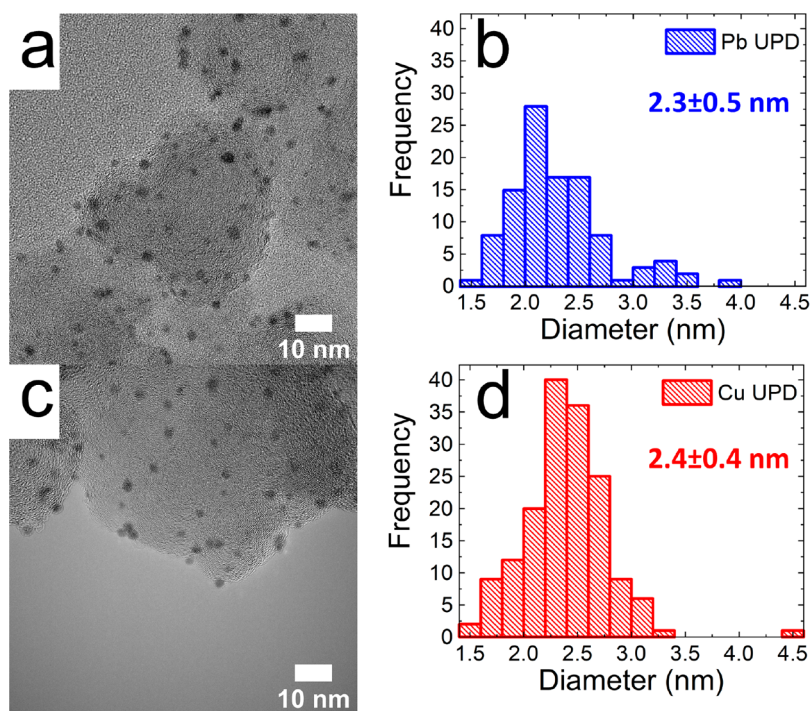
Figure 2. (a,c) Representative TEM micrographs for AuPt DENs synthesized using (a) Pb UPD/Pt GE and (c) Cu UPD/Pt GE. (b, d) Size distributions associated with (a) and (c), respectively. Each distribution was obtained by sizing 200 randomly selected NPs.

representing one complete ML (1.0 ML). Multiplying the Pb/Au_i SA ratio (0.86) by the number of surface atoms on a G6-$NH_2(Au_{147})$ DEN (92) yields 79 Pb atoms = 0.49 ML. Using this definition and on the basis of nine independent experiments, the Pb coverage on the G6-$NH_2(Au_{147})$ DENs is 0.49 ± 0.03 ML. There is one caveat regarding this value, however. As shown in Figure S2, the size of the G6-$NH_2(Au_{147})$ DENs increases from 1.7 ± 0.3 to 1.9 ± 0.4 nm after 20 electrochemical cleaning scans (i.e., just prior to Pb UPD). Hence, 0.49 ML represents our best estimate of the Pb coverage within the context of the error associated with the TEM size-distribution data.

As discussed in the Experimental Section, the synthesis of AuPt DENs via Pb UPD/Pt GE proceeds in two steps. First, Pb UPD on the G6-$NH_2(Au_{147})$ DENs was performed by holding the electrode potential at −0.15 V for 300 s. Second, K_2PtCl_4 was introduced into the cell to initiate Pt GE with the electrode held at the open circuit potential. This step results in the replacement of the Pb UPD shell with Pt. Note that we refer to this material as AuPt rather than Au@Pt to indicate that at this stage in the analysis we are uncertain as to its structure (e.g., core@shell, random alloy, or a hybrid).

Figure 2a is a TEM micrograph of the AuPt DENs synthesized by Pb UPD/Pt GE, and Figure 2b is the corresponding size-distribution histogram. The average size of the AuPt NPs is 2.3 ± 0.5 nm, which is close to the size (2.1 nm) of a perfect 309-atom cuboctahedral NP consisting of a 147-atom Au core and a 162-atom Pt shell.[16] The size is also consistent with those reported previously for AuPt DENs prepared by UPD/Pt GE onto Au DENs.[16,19,42]

Figure 1a shows representative CVs before (black trace) and after (red trace) Pb UPD/Pt GE. As mentioned earlier, only a single peak, corresponding to AuO_x reduction, is observed (at ∼1.1 V) prior to Pb UPD/Pt GE. After UPD/GE, however, the area under the AuO_x reduction wave decreases and two

new features arise: a PtO_x reduction peak and hydrogen adsorption/desorption waves (Pt hydride waves). The PtO_x reduction peak is centered at 0.66 V, and Pt hydride waves are observed negative of ∼0.30 V.

As discussed in Section S1, the Pt coverage was estimated to be 1 − (Au_f/Au_i). As previously mentioned, Au_i (0.28 cm^2) is the Au SA before UPD/Pt GE. Au_f is the Au SA after UPD/Pt GE, determined in the same way as Au_i, except that the red trace of Figure 1a was used to calculate Au_f = 0.14 cm^2. The average estimated Pt coverage (from nine independent measurements) is therefore 0.50 ± 0.04 ML. This value is in good agreement with the experimental Pb coverage (0.49 ± 0.03 ML), suggesting the complete exchange of Pt for Pb during GE.

Synthesis and Characterization of AuPt DENs Prepared via Cu UPD/Pt GE. Cu UPD was carried out as described in the Experimental Section and in a similar fashion to Pb UPD. Prior to UPD, however, a control CV (Figure S3) was obtained in the potential range used for Cu UPD to ensure the absence of contaminants and competing processes. An analogous CV was not obtained prior to Pb UPD because the hydrogen evolution reaction (HER) occurs on naked Au within the relevant potential range.[18] In the presence of Pb^{2+}, however, scanning the potential in this range coats Au with Pb prior to the onset of the HER (Figure S4).

Cu UPD (black trace in Figure 1c) was carried out in a N_2-purged solution containing 5.0 mM $CuSO_4$ and 0.10 M $HClO_4$. The Au DEN-modified GCE was held at a potential of 0.70 V for 300 s and then scanned from 0.70 to 0.85 to 0.30 V at a rate of 10 mV/s. The corresponding LSV (red trace in Figure 1c) was recorded like the Pb LSV, but a deposition potential of 0.32 V was used in this case. As with Pb UPD, the Cu UPD CV and LSV overlay almost perfectly, confirming the absence of bulk Cu deposition. For the Cu UPD CV, two deposition peaks are centered at ∼0.45 and 0.34 V and two
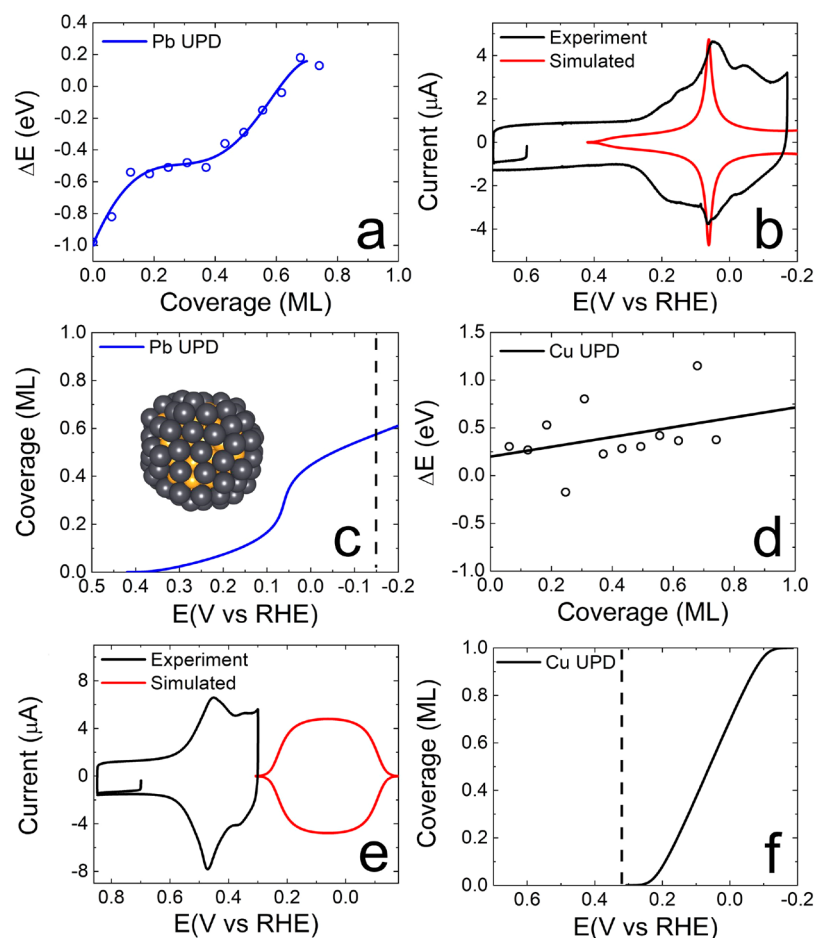
Figure 3. (a, d) Differential binding energy (ΔE) as a function of coverage for (a) Pb UPD and (d) Cu UPD. UPD becomes unfavorable for ΔE values greater than 0. (b, e) Comparison of experimental (black traces) and theoretically simulated (red traces) UPD CVs for (b) Pb and (e) Cu. (c, f) UPD coverage as a function of applied potential for (c) Pb and (f) Cu. The dashed lines indicate the experimental UPD potentials. The inset in (c) is an atomic model of 96 Pb atoms covering an Au_{147} core at the maximum allowed coverage of 0.59 ML.

stripping peaks are centered at 0.37 and 0.47 V. The deposition and stripping potentials are in good agreement with previous reports of Cu UPD onto Au_{147} DENs.[15,23,42,44]

In previous reports of Cu UPD onto comparably sized Pt DENs,[29,30] the presence of two Cu UPD peaks was used as evidence of a facet-by-facet mechanism with Cu depositing sequentially onto (100) and (111) facets.[29] However, just like Pb UPD, this mechanism is likely an oversimplification for two primary reasons. First, as discussed in the Pb UPD section, there is extensive atomic sharing between facets for NPs in the size range of DENs. Second, SO_4^{2-} and Cu^{2+} coadsorb onto Au in sulfate-containing media, and under these conditions, Cu UPD onto bulk Au(111) has been reported to produce two UPD peaks.[18] The first peak corresponds to 0.67 ML of Cu coadsorbed with 0.33 ML of SO_4^{2-}, and the second peak is characteristic of a full Cu ML having 0.33 ML of SO_4^{2-} adsorbed atop the Cu. As discussed in Section S2 in the Supporting Information, Cu UPD experiments carried out using G6-NH$_2$(Au_{147}) DENs in electrolyte solutions with and without SO_4^{2-} confirm this mechanism. The Cu UPD results presented here highlight the important role of SO_4^{2-} ligands in the UPD process. This point will be discussed later in more detail.

The fractional Cu ML coverage was calculated in the same way as the Pb coverage, with some additional considerations related to the coadsorption of Cu^{2+} and SO_4^{2-} (Section S3).

Using a charge density of 405 $\mu C/cm^2$,[15] the Cu SA is 0.31 cm^2. The Au SA prior to Cu UPD/Pt GE (Au_i) is 0.31 cm^2. Thus, the Cu/Au_i SA ratio is 1.0. On the basis of six independent measurements and assuming that the G6-NH$_2$(Au_{147}) DEN core is a perfect 147-atom cuboctahedron, the Cu coverage is 0.57 ± 0.05 ML.

The synthesis of AuPt DENs via Cu UPD/Pt GE followed essentially the same procedure as Pb UPD/Pt GE with the exception that the UPD potential was 0.32 V. Figure 2c is a TEM micrograph of the resulting AuPt DENs, and Figure 2d is the corresponding size-distribution histogram. The data show that the size of the AuPt DENs is 2.4 ± 0.4 nm, which is essentially the same as the AuPt NPs prepared by Pb UPD/Pt GE (2.3 ± 0.5 nm).

Figure 1d compares CVs obtained before (black trace) and after (red trace) Cu UPD/Pt GE. After Cu UPD/Pt GE, the PtO_x reduction (0.60 V) and Pt hydride (negative of ~0.30 V) peaks are apparent, and the AuO_x reduction peak (at ~1.1 V) is attenuated. These changes are qualitatively similar to those observed for Pb UPD/Pt GE (Figure 1a).

Pt coverage was estimated in the same way as for Pb UPD/Pt GE: 1-(Au_f/Au_i). For Cu UPD/Pt GE, Au_i and Au_f equal 0.31 and 0.092 cm^2, respectively. On the basis of six independent measurements, the average Pt coverage is 0.70 ± 0.01 ML. This value is higher than expected on the basis of 1:1 exchange of the experimentally determined Cu coverage

(0.57 ± 0.05 ML) for Pt. This might be a consequence of the fact that the charge density values used to calculate the Cu and Au SAs (405 and 390 $\mu C/cm^2$, respectively) are only strictly appropriate for bulk Au,[15] and they might not be accurate for small NPs.[15] We note, however, that the (Au_f/Au_i) term used to calculate the Pt coverage $(1 - (Au_f/Au_i))$ is independent of charge density and therefore the Pt coverage here might be more accurate than the Cu coverage.

One final point. Here, we used different concentrations of $Pb(NO_3)_2$ (1.0 mM) and $CuSO_4$ (5.0 mM) for the UPD processes. This was done to be consistent with previous publications.[16,19,42] Note, however, that Figure S5 shows that the use of 1.0 mM $Cu(NO_3)_2$, chosen to match the Pb concentration and counterion, yields results similar to those for 5.0 mM $CuSO_4$ in terms of Pt coverage (0.76 ± 0.03 vs 0.70 ± 0.01 ML for 5.0 mM $CuSO_4$).

Comparison of AuPt DENs Prepared by Pb UPD/Pt GE and Cu UPD/Pt GE. The CVs for the AuPt DENs prepared using the Pb UPD/Pt GE and Cu UPD/Pt GE methods differ in two respects: (1) the PtO_x reduction peak potential and (2) the surface coverage of Pt. With regard to (1), the PtO_x reduction peak is 60 mV more negative for the AuPt DENs synthesized using Cu UPD/Pt GE relative to those prepared using Pb UPD/Pt GE, suggesting differences in surface structure. In the case of point (2), the Pt coverage for the AuPt DENs is ~0.20 ML greater for the Cu UPD/Pt GE method than for the Pb case. This suggests that these two methods are not interchangeable and could, for example, lead to materials having very different electrocatalytic properties. Importantly, and as we will discuss in the next section, this difference in Pt coverage is predicted by theory. Specifically, theory suggests lower Pt coverage (0.59 ML) and a surface alloylike structure for Pb UPD/Pt GE. A higher Pt coverage (1.0 ML) and a more ideal core@shell Au@Pt structure are predicted for Cu UPD/Pt GE.

Pb UPD Simulations. Pb atoms were placed randomly (as opposed to facet-by-facet) and incrementally onto the surface of a cuboctahedral Au_{147} NP to simulate the Pb UPD process on $G6-NH_2(Au_{147})$ DENs. It should be noted that equilibration at 300 K significantly deforms the original cuboctahedral Au_{147} NP structure. Specifically, the (100) facets reconstruct in a way that makes most of the surface close-packed. This process eliminates the distinction between (100) and (111) facets, and the final surface can be best described as (111)-like. In total, 13 Pb_x/Au_{147} ($x = 1$ to 120 with an incremental step size of 10 Pb atoms) structures were simulated. Each structure was equilibrated at 300 K, using the MD simulation method described in the Experimental Section and was then relaxed to its equilibrium state at 0 K. The equilibrated, relaxed structures are shown in Figure S6. Figure 3a shows the differential binding energies (ΔE) of the deposited Pb atoms that were calculated for these structures as a function of Pb coverage. The ΔE values quickly increase with Pb coverage from 0 to 0.2 ML. At 0.2 ML, a plateau is reached, and it extends until 0.4 ML, after which ΔE rapidly increases again. Importantly, Figure 3a suggests that Pb UPD is energetically favorable up to ~0.60 ML coverage, after which ΔE becomes positive.

The behavior of ΔE as a function of Pb coverage can be interpreted by tracking changes in the coordination numbers (CNs) of the deposited Pb adatoms (Figure S7). The first data point on this plot corresponds to the adsorption of 1 Pb atom. Initially, this single Pb atom is highly coordinatively

unsaturated. As a result, the Pb adatom induces local structural reconstruction of the AuNP to stabilize its adsorption. As shown in the second frame of Figure S6 (Pb_1/Au_{147}), this AuNP reconstruction results in an average Pb–Au CN of 6. As the Pb coverage increases, however, the average Pb–Au CN decreases from 6 to 3 and the average Pb–Pb CN increases from 0 to 5.

The foregoing behavior can be explained by considering the effects of Pb island formation on the underlying Au surface. As Pb island growth proceeds, the increase in the Pb–Pb CN alleviates the reliance on Au lattice deformation to meet the Pb atom coordination requirements. Summing the Pb–Au and Pb–Pb CNs, the total Pb CN (Pb–M) increases from 6 to 8 as a function of Pb coverage. The opposing Pb–Pb and Pb–Au CN trends result in slowed growth of the Pb–M CN between 0.2 and 0.4 ML, thereby accounting for the plateau in ΔE (Figure 3a) for those coverages. The rapid increase in ΔE beyond 0.4 ML in Figure 3a can be attributed to the fact that as the Pb–Pb CN continues to increase and the Pb–Au CN continues to decrease, it becomes more difficult to deposit additional Pb atoms. This feature arises from the fact that Pb binds more strongly to Au than it does to itself (this is why Pb UPD is possible on Au).

The simulated Pb UPD CV (Figure 3b) is based on the calculated ΔE value. The main peak corresponds to the plateau in the plot of ΔE as a function of Pb coverage (Figure 3a). This peak is centered at 0.06 V and aligns well with the corresponding peak in the experimental CV (0.04 V; Figure 1b). In the experimental Pb UPD CV, there are smaller peaks before and after the main peak. The simulated CV predicts flat currents rather than peaks in these two regions due to the rapid increase in ΔE vs Pb coverage. This discrepancy might be due to the limited resolution of the simulations because the Pb coverage was increased using a step size of 10 Pb atoms. Accordingly, complete details about the ΔE landscape were not captured. Additionally, the time scale associated with MD simulations is limited to picoseconds. As a result, it was not possible to simulate the reorganization of Pb adatoms on the Au_{147} surface through diffusion, which might occur at longer times. Finally, there is some structural polydispersity in the DENs that could introduce nonidealities into the experimental data. Some or all of these factors could affect the correlation between experiment and simulation.

As shown in Figure 3c, the predicted Pb coverage as a function of applied potential can be determined by integrating the simulated CV in Figure 3b. The vertical dashed line indicates the experimental potential, −0.15 V, that was used for Pb UPD onto the $G6-NH_2(Au_{147})$ DENs. At this potential, 96 Pb atoms are predicted to deposit on Au_{147}, corresponding to a coverage of 0.59 ML (using the definition of fractional ML coverage defined in the previous sections (1.0 ML = 162 atoms)). We note that the atomic structure in the inset of Figure 3c represents Pb_{100}/Au_{147} rather than Pb_{96} because, as mentioned earlier, a coverage step size of 10 Pb atoms was used in the simulations. The Pb coverage predicted for Pb UPD at −0.15 V is in good agreement with both the experimentally determined Pb coverage (0.49 ± 0.03 ML) and the Pt coverage (0.50 ± 0.04 ML) after Pt GE.

Although the Pb coverage predicted in the present report (0.59 ML) is similar to our earlier publication detailing Pb UPD on Au_{147} (0.63 ML),[16] we obtain a more realistic picture of the Pb UPD process on Au_{147} using DFT-MD in the current study. As alluded to earlier, DFT-MD reveals that the

cuboctahedral Au_{147} NPs reconstruct spontaneously at 300 K, leaving no distinct (100) and (111) facets on their surfaces. Consequently, the previously reported facet-by-facet growth mode is not appropriate. Instead, we envision that Pb adatoms deposit randomly on the reconstructed Au_{147} surface. Equilibration of the Pb_x/Au_{147} structures at 300 K makes it possible to consider rearrangement of the atoms at finite temperature after each Pb atom is deposited. The agreement between the simulated and experimental CVs supports the validity of this new structural model and provides a higher degree of mechanistic insight into the Pb UPD process.

Figure 4a,b show the structures predicted before and after the Pt GE step. For these simulations, the deposited Pb atoms
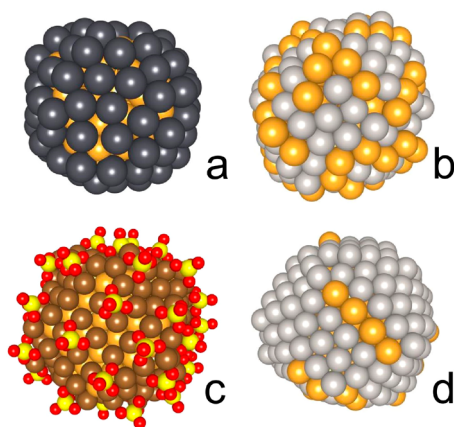
Figure 4. Atomic models for Au_{147} DENs. (a, c) $Au_{147}@x$, where (a) x = Pb and (c) x = Cu with coadsorbed $SO_4^{\delta-}$. (b, d) AuPt formed by performing Pt GE on the NPs in (a) and (c), respectively.

in Pb_{100}/Au_{147} were replaced with Pt. The new structure was then equilibrated at 300 K for 20 ps. After Pt GE, a significant number of Au atoms are still on the NP surface. Fewer Pb atoms than Pt atoms are required for complete Au_{147} surface coverage because Pt atoms are smaller than Pb atoms. Thus, upon Pt GE, surface coverage of the AuNP decreases. As a result, the final structure more closely resembles a surface alloy than the core@shell Au@Pt structure that was anticipated.

Cu UPD Simulations. Simulation of the Cu UPD CV followed a similar approach to that of Pb UPD. The equilibrated, relaxed atomic structures for naked Au_{147} with deposited Cu are shown in Figure S8. In all cases, the deposited Cu atoms incorporate (alloy) into the Au_{147} core after equilibration to increase their CNs. This scenario differs from that of Pb UPD, where all UPD atoms are predicted to be adsorbed on top of the Au atoms. This difference arises from the fact that Pb atoms are larger than Cu atoms. Specifically, although PbAu alloys are stronger than CuAu alloys, PbAu alloys are kinetically more difficult to form because there is a larger lattice mismatch between Pb and Au lattices.[18] Furthermore, the ΔE values of Cu adatoms (Figure 3d) are positive throughout the entire range (0 to 1.0 ML) of Cu coverage. Therefore, the theoretical simulations predict that Cu UPD on naked Au_{147} NPs should not occur within the potential range used to obtain the CV shown in Figure 1c. This means that Cu UPD in the simulated CV (Figure 3e) requires a significant overpotential and thus occurs in a more negative potential range than the experimental CV. This point is further emphasized in Figure 3f, where the Cu UPD onset potential (~0.20 V) and the potential corresponding to a full Cu ML

(~-0.10 V) are predicted to be ~250−440 mV more negative than the experimentally observed Cu UPD peak potentials (~0.45 and 0.34 V, respectively).

The discrepancy between experiment and theory outlined above has been previously reported[29,65,66] and attributed to neglecting ligand effects in the theoretical calculations. The calculations for Cu UPD described up until this point were carried out by assuming that Cu UPD on the surface of Au_{147} NPs results exclusively in the deposition of Cu. However, experimental studies have shown that anionic ligands coadsorb with Cu on bulk Au in the UPD potential range.[18] For example, STM studies[18] have shown that the first of two peaks in the Cu UPD CV for Au(111) corresponds to 0.67 ML of Cu and 0.33 ML of $SO_4^{\delta-}$ ($SO_4^{\delta-}$ is used to denote uncertainty in the exact SO_4 charge upon adsorption). A full Cu ML can be obtained, but it requires scanning the potential further negative (with respect to the second peak). As we describe next, the gap between the experimental and theoretical results for Cu UPD on Au_{147} narrows once ligand and electric double layer (EDL) effects are taken into account.

Influence of Ligand/EDL Effects on the Cu UPD Simulations. To predict the correct equilibrium potentials for Cu UPD on Au, calculations were performed to simulate the EDL under constant potential conditions using the double reference method described in the Experimental Section. The two structures used were those determined experimentally for Cu UPD on Au(111) in the presence of $SO_4^{\delta-}$.[18] The two structures correspond to the two peaks in the Cu UPD CV for Au(111). The first structure is Au(111) with a partial Cu ML (Figure 5a) consisting of 0.67 ML of Cu coadsorbed with 0.33 ML of $SO_4^{\delta-}$. The second structure is Au(111) having a full Cu ML and 0.33 ML of $SO_4^{\delta-}$ coadsorbed on top of the Cu (Figure 5b). For simplicity, we refer to these two models as partial ML and full ML, respectively.

Figure 5c,d shows the total energies of naked Au(111) and Au(111) with coadsorbed Cu and $SO_4^{\delta-}$ as a function of potential. The total energies of these interfaces display quadratic shapes because they act as capacitors. For naked Au(111) (Figure 5c, red trace), the predicted potential of zero charge (PZC) is 0.42 V. For the partial ML structure (Figure 5c, blue trace), the PZC shifts to a much higher value (3.6 V) than naked Au(111) due to electron transfer from the metal surface to adsorbed $SO_4^{\delta-}$.

As a result of the PZC shift, the adsorption energy (the difference between the blue and red traces in Figure 5c,d) becomes more positive at more positive potentials. In other words, as the applied potential is scanned in the negative direction during the UPD process, $CuSO_4$ coadsorption becomes more and more stable. This variation in adsorption energy as a function of potential is mainly caused by differences in the number of electrons residing on the $CuSO_4$ coadsorption interface vs the naked Au(111) surface. At more negative potentials, the $CuSO_4$ coadsorption interface accommodates more electrons than the naked Au(111) surface. This in turn leads to greater stability of the $CuSO_4$ coadsorption interface at more negative potentials. Thus, for the potential used for Cu UPD (0.32 V), the surface of the partial ML structure harbors significantly more negative charge than naked Au(111). Similar conclusions are obtained for the full ML structure (Figure 5d).

Using the calculated, potential-dependent binding energies of the $CuSO_4$ coadsorption layers, we evaluated the reaction free energy (ΔG) of the Cu UPD process (Figure 5e) when
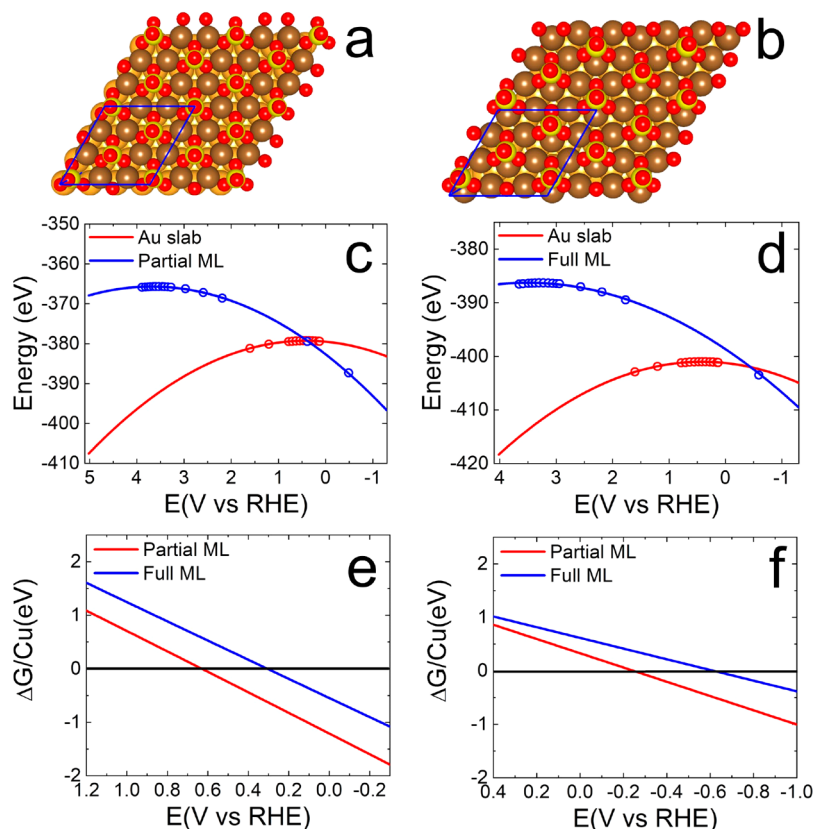
Figure 5. (a, b) Models of extended Au(111) surfaces with (a) partial and (b) full Cu MLs. The partial Cu ML consists of 0.67 ML of Cu coadsorbed with 0.33 ML of $SO_4^{\delta-}$. A layer of $SO_4^{\delta-}$ is adsorbed on top of the full Cu ML. The gold, brown, yellow, and red spheres correspond to Au, Cu, S, and O atoms, respectively. (c, d) Plots used for determining the potential of zero charge (PZC) for naked Au(111) (red traces) and Au(111) with coadsorbed Cu and $SO_4^{\delta-}$ (blue traces) for (c) partial and (d) full Cu MLs. (e, f) Free energy (ΔG) as a function of applied electrode potential for Cu UPD onto an Au(111) slab (e) when both ligand and electric double layer (EDL) effects are taken into account and (f) when only ligand effects are considered.

both EDL and ligand effects are taken into account. The predicted equilibrium potentials for the partial (red trace) and full (blue trace) Cu MLs are 0.63 and 0.31 V, respectively. These two potentials agree reasonably well with those associated with experimentally determined Cu UPD onto Au(111) in 0.10 M H_2SO_4 (0.53 and 0.35 V).[67] They are also in reasonable agreement with the two peaks in the experimental Cu UPD CV (Figure 1c) for the G6-$NH_2(Au_{147})$ DENs, which are centered at 0.45 and 0.34 V. As mentioned previously, Figure 1c was recorded in 10.0 mL of 0.10 M $HClO_4$ containing 5.0 mM $CuSO_4$. Thus, the SO_4^{2-} concentration was in excess with respect to the AuNPs on the working electrode (6.0 μL of an ink containing 2.0 μM G6-$NH_2(Au_{147})$ DENs). To determine if 5.0 mM SO_4^{2-} was indeed sufficient to induce coadsorption effects, a Cu UPD CV was recorded at higher SO_4^{2-} concentration (0.10 M H_2SO_4; Figure S2.1a). The peak positions in Figure S2.1a (0.44 and 0.30 V) are similar to those in Figure 1c, indicating that 5.0 mM SO_4^{2-} is adequate to observe the effect of $SO_4^{\delta-}$ on Cu UPD. Note that our prior report of Cu UPD potentials on Pt DENs[29] considered ligand effects but not the EDL.

The importance of the EDL calculations is underscored by comparing the results in Figure 5e to those obtained using the $CuSO_4$ binding energies calculated at the PZC (Figure 5f). The latter calculations were designed to eliminate EDL effects, thereby isolating ligand effects. The calculated equilibrium potentials for the two stages of Cu UPD (−0.25 V and −0.62

V) are much more negative in the absence of EDL considerations and are significantly shifted from the experimental values (by ~560−960 mV). In fact, they are even worse than predicted for a naked Au_{147} NP (Figure 3f). The large errors in the predicted equilibrium potentials for Cu UPD are due to the fact that the adsorption energies calculated from the difference in the energies of the naked Au(111) surface and the $CuSO_4$ coadsorption interface, at the PZC (zero charge calculations), are very positive. Thus, the most accurate Cu UPD results are obtained when both ligand and EDL effects are taken into account.

Given that the Pb UPD and Cu UPD experiments used different anions ($Pb(NO_3)_2$ and $CuSO_4$), we also evaluated the ligand and EDL effects of NO_3 for Cu UPD (Figure S9). As for the $CuSO_4$ case, the PZC for Au(111) is significantly shifted when Cu and $NO_3^{\delta-}$ are coadsorbed (Figure S9a,b). Furthermore, Figure S9c shows that the PZC shift for $Cu(NO_3)_2$ translates to predicted partial (0.62 V) and full (0.33 V) Cu ML potentials that are very similar to the corresponding potentials predicted for $CuSO_4$ (0.63 and 0.31 V). Indeed, the potential predicted for a full Cu ML is very close to that experimentally observed for $Cu(NO_3)_2$ (0.32 V, Figure S2.1c). Thus, overall, $SO_4^{\delta-}$ and $NO_3^{\delta-}$ provide similar ligand/EDL effects for Cu UPD on Au(111).

Notably, the comparison of $CuSO_4$ and $Cu(NO_3)_2$ suggests that the mere presence of ligands, regardless of their identity, profoundly impacts the EDL structure and thus the Au(111)

PZC associated with Cu UPD. In other words, our results suggest that the presence of any ligand will shift the Cu UPD potentials from those determined on naked Au. These calculations further highlight the differences between Pb UPD, which does not require the consideration of either ligand or EDL effects to obtain agreement between experiment and theory, and Cu UPD, which is markedly altered by these effects. This difference has been observed previously[68] and likely arises from the fact that the Pb ML is charge-neutral, whereas the Cu ML possesses residual charge. Therefore, the similarity of the ligand/EDL effects for $SO_4^{\delta-}$ and $NO_3^{\delta-}$, along with the fact that Pb is relatively insensitive to ligand effects,[68] justifies the comparison of AuPt NP structures synthesized using $Pb(NO_3)_2$ and $CuSO_4$.

Theoretical NP Models for Cu UPD/Pt GE. The calculations detailed in the previous section confirm that $CuSO_4$ coadsorption structures form on the Au(111) surfaces during the UPD process. We now turn to a consideration of the AuNPs. In the experimental Cu UPD CV for G6-$NH_2(Au_{147})$ DENs (Figure 1c), a peak (highlighted by the arrow) resembling the second stage (~1.0 ML Cu) of Cu UPD onto Au(111) is observed at 0.34 V. This peak is more pronounced at higher SO_4^{2-} concentration (Figure S2.1a) and is absent when $Cu(NO_3)_2$ is used (Figure S2.1c), confirming its association with SO_4^{2-}. Hence, we assume that there is full coverage of Cu on the surface of the AuNP.

Accordingly, we built a full Cu shell model containing 162 Cu atoms on an Au_{147} NP and evenly placed 44 $SO_4^{\delta-}$ ligands (~0.3 ML) on top of the Cu layer. The equilibrated structure is shown in Figure 4c. Unlike the Pb coverage, the theoretically predicted Cu coverage (1.0 ML) differs from that determined by experiment (0.57 ± 0.05 ML). This result is not necessarily surprising for the following reasons. First, sub-ML Cu coverages have previously been reported on AuNPs.[14,28] Second, our previous reports of Cu UPD on Au_{147} DENs[15] and comparably sized Pt DENs[29,30] have revealed ratios of Cu to surface Au or Pt atoms of 0.74−1.0; these ratios correspond to fractional ML coverages significantly lower than 1.0 ML (0.41−0.63 ML depending on the core size). These discrepancies were previously attributed to Cu UPD being energetically unfavorable on corner and edge sites.[15,29,30] Third, a completely naked Au_{147} NP model was used in our theoretical prediction of a full Cu ML (Figure 3f). As we have demonstrated, ligand and EDL effects have significant implications for Cu UPD. It is possible that these effects impacted the extent of Cu coverage.

Figure 4d shows the AuPt NP model formed by replacing the $CuSO_4$ layer (from Figure 4c) with Pt atoms and allowing the structure to equilibrate. As indicated, the shell consists almost entirely of Pt, which is in stark contrast to the surface alloylike AuPt structure generated using Pb UPD/Pt GE (Figure 4b). Although the former structure predicts Pt coverage that is higher than experimentally obtained (~0.70 ML Pt coverage) for Cu UPD/Pt GE, the two UPD/Pt GE methods display a significant difference (~0.20 ML) in Pt coverage. Thus, both theory and experiment suggest that Pb UPD/Pt GE and Cu UPD/Pt GE generate different AuPt structures. Cu UPD/Pt GE is predicted to afford a more ideal core@shell AuPt structure, and Pb UPD/Pt GE yields an AuPt structure that more closely resembles a surface alloy. Importantly, the Pt ensembles on the NP surfaces differ. As we will show in a forthcoming report, differences in ensemble

effects for these NPs lead to distinct catalytic signatures for FAO.

SUMMARY AND CONCLUSIONS

We have used both experiment and theory to analyze Pb and Cu UPD on ~1.7 nm AuNPs and the AuPt structures that result after galvanic exchange (GE) of the UPD layer for Pt. Experimental Pb (0.49 ML) and Pt (0.50 ML) coverages are both close to values predicted by density functional theory-molecular dynamics (DFT-MD; 0.59 ML). DFT-MD reveals that the AuNPs spontaneously reconstruct from cuboctahedral to a (111)-like structure prior to UPD. In the case of Pb, this results in the random electrodeposition of Pb onto the Au surface. This mechanism is a consequence of opposing trends in Pb−Pb and Pb−Au coordination numbers as a function of Pb coverage. Cu UPD is more complex, and agreement between theory and experiment takes into account ligand effects (e.g., SO_4^{2-} present as the electrolyte) and the electric double layer. Importantly, AuPt structures formed on Pt GE were found to differ markedly depending on the UPD metal. Specifically, cyclic voltammetry indicates that the Pt coverage is ~0.20 ML greater for Cu UPD/Pt GE (0.70 ML) than for Pb UPD/Pt GE (0.50 ML). This difference was corroborated by DFT-MD theoretical predictions and was attributed to dissimilar Pb and Cu atomic sizes as well as the higher impact of ligand and EDL effects on Cu UPD than on Pb UPD. Finally, DFT-MD calculations predicted the formation of surface alloy and core@shell structures for Pb UPD/Pt GE and Cu UPD/Pt GE, respectively.

Moving forward, we wish to better understand the generality of these experimental and theoretical results: can they be applied to other UPD metals and differently sized cores? The answers to these questions are directly relevant to fundamental questions regarding the stability and phase behavior of metal NPs. The results of our studies aimed at answering these questions will be reported in due course.

ASSOCIATED CONTENT

⑤ Supporting Information

The Supporting Information is available free of charge at https://pubs.acs.org/doi/10.1021/acs.langmuir.9b03192.

> UV−vis and TEM analysis of G6-$NH_2(Au_{147})$DENs; the effect of electrochemical pretreatment on NP size; representative background CV recorded in the potential range relevant to Cu UPD; effect of Pb UPD on CVs of Au DEN-modified electrodes; Pt coverage for UPD/Pt GE with 1 mM $Cu(NO_3)_2$; equilibrated and relaxed structures for Pb adsorption onto Au_{147} NPs; predicted Pb coordination numbers as a function of Pb coverage on Au_{147} NPs; simulated Cu deposition onto Au_{147} NPs in the absence of ligands; ligand and electric double layer effects for $Cu(NO_3)_2$ UPD on an Au(111) slab; estimation of Pt coverage; effects of adsorbates on Cu UPD on G6-$NH_2(Au_{147})$ DENs; Cu coverage estimation (PDF)

AUTHOR INFORMATION

Corresponding Authors
*E-mail: henkelman@utexas.edu.
*E-mail: crooks@cm.utexas.edu.

ORCID ⓘ

Graeme Henkelman: 0000-0002-0336-7153

Richard M. Crooks: 0000-0001-5186-4878

Author Contributions

‖These authors contributed equally.

Notes

The authors declare no competing financial interest.

■ REFERENCES

(1) Zhang, Y.; Hsieh, Y.-C.; Volkov, V.; Su, D.; An, W.; Si, R.; Zhu, Y.; Liu, P.; Wang, J. X.; Adzic, R. R. High Performance Pt Monolayer Catalysts Produced via Core-Catalyzed Coating in Ethanol. *ACS Catal.* **2014**, *4*, 738−742.

(2) Sasaki, K.; Naohara, H.; Cai, Y.; Choi, Y. M.; Liu, P.; Vukmirovic, M. B.; Wang, J. X.; Adzic, R. R. Core-Protected Platinum Monolayer Shell High-Stability Electrocatalysts for Fuel-Cell Cathodes. *Angew. Chem., Int. Ed.* **2010**, *49*, 8602−8607.

(3) Shao, M.; Chang, Q.; Dodelet, J.-P.; Chenitz, R. Recent Advances in Electrocatalysts for Oxygen Reduction Reaction. *Chem. Rev.* **2016**, *116*, 3594−3657.

(4) Guo, S.; Zhang, S.; Sun, S. Tuning Nanoparticle Catalysis for the Oxygen Reduction Reaction. *Angew. Chem., Int. Ed.* **2013**, *52*, 8526−8544.

(5) Zhang, L.; Iyyamperumal, R.; Yancey, D. F.; Crooks, R. M.; Henkelman, G. Design of Pt-Shell Nanoparticles with Alloy Cores for the Oxygen Reduction Reaction. *ACS Nano* **2013**, *7*, 9168−9172.

(6) Anderson, R. M.; Yancey, D. F.; Zhang, L.; Chill, S. T.; Henkelman, G.; Crooks, R. M. A Theoretical and Experimental Approach for Correlating Nanoparticle Structure and Electrocatalytic Activity. *Acc. Chem. Res.* **2015**, *48*, 1351−1357.

(7) Zhang, L.; Henkelman, G. Computational Design of Alloy-Core@Shell Metal Nanoparticle Catalysts. *ACS Catal.* **2015**, *5*, 655−660.

(8) Turner, M.; Golovko, V. B.; Vaughan, O. P.; Abdulkin, P.; Berenguer-Murcia, A.; Tikhov, M. S.; Johnson, B. F.; Lambert, R. M. Selective Oxidation with Dioxygen by Gold Nanoparticle Catalysts Derived from 55-Atom Clusters. *Nature* **2008**, *454*, 981−983.

(9) An, K.; Somorjai, G. A. Size and Shape Control of Metal Nanoparticles for Reaction Selectivity in Catalysis. *ChemCatChem* **2012**, *4*, 1512−1524.

(10) Roduner, E. Size Matters: Why Nanomaterials Are Different. *Chem. Soc. Rev.* **2006**, *35*, 583−592.

(11) Myers, V. S.; Weir, M. G.; Carino, E. V.; Yancey, D. F.; Pande, S.; Crooks, R. M. Dendrimer-Encapsulated Nanoparticles: New Synthetic and Characterization Methods and Catalytic Applications. *Chem. Sci.* **2011**, *2*, 1632−1646.

(12) Dai, Y.; Chen, S. Oxygen Reduction Electrocatalyst of Pt on Au Nanoparticles through Spontaneous Deposition. *ACS Appl. Mater. Interfaces* **2015**, *7*, 823−829.

(13) Ahn, S. H.; Liu, Y.; Moffat, T. P. Ultrathin Platinum Films for Methanol and Formic Acid Oxidation: Activity as a Function of Film Thickness and Coverage. *ACS Catal.* **2015**, *5*, 2124−2136.

(14) Yu, Y.; Hu, Y.; Liu, X.; Deng, W.; Wang, X. The Study of Pt@Au Electrocatalyst Based on Cu Underpotential Deposition and Pt Redox Replacement. *Electrochim. Acta* **2009**, *54*, 3092−3097.

(15) Yancey, D. F.; Carino, E. V.; Crooks, R. M. Electrochemical Synthesis and Electrocatalytic Properties of Au@Pt Dendrimer-Encapsulated Nanoparticles. *J. Am. Chem. Soc.* **2010**, *132*, 10988−10989.

(16) Yancey, D. F.; Zhang, L.; Crooks, R. M.; Henkelman, G. Au@Pt Dendrimer Encapsulated Nanoparticles as Model Electrocatalysts for Comparison of Experiment and Theory. *Chem. Sci.* **2012**, *3*, 1033−1040.

(17) Peng, L.; Gan, L.; Wei, Y.; Yang, H.; Li, J.; Du, H.; Kang, F. Pt Submonolayers on Au Nanoparticles: Coverage-Dependent Atomic Structures and Electrocatalytic Stability on Methanol Oxidation. *J. Phys. Chem. C* **2016**, *120*, 28664−28671.

(18) Herrero, E.; Buller, L. J.; Abruna, H. D. Underpotential Deposition at Single Crystal Surfaces of Au, Pt, Ag, and Other Materials. *Chem. Rev.* **2001**, *101*, 1897−1930.

(19) Iyyamperumal, R.; Zhang, L.; Henkelman, G.; Crooks, R. M. Efficient Electrocatalytic Oxidation of Formic Acid Using Au@Pt Dendrimer-Encapsulated Nanoparticles. *J. Am. Chem. Soc.* **2013**, *135*, 5521−5524.

(20) Brankovic, S. R.; Wang, J. X.; Adzic, R. R. Metal Monolayer Deposition by Replacement of Metal Adlayers on Electrode Surfaces. *Surf. Sci.* **2001**, *474*, L173−L179.

(21) Liu, Y.; Gokcen, D.; Bertocci, U.; Moffat, T. P. Self-Terminating Growth of Platinum Films by Electrochemical Deposition. *Science* **2012**, *338*, 1327−1330.

(22) Liu, Y.; Hangarter, C. M.; Garcia, D.; Moffat, T. P. Self-Terminating Electrodeposition of Ultrathin Pt Films on Ni: An Active, Low-Cost Electrode for H2 Production. *Surf. Sci.* **2015**, *631*, 141−154.

(23) Lapp, A. S.; Duan, Z.; Marcella, N.; Luo, L.; Genc, A.; Ringnalda, J.; Frenkel, A. I.; Henkelman, G.; Crooks, R. M. Experimental and Theoretical Structural Investigation of AuPt Nanoparticles Synthesized Using a Direct Electrochemical Method. *J. Am. Chem. Soc.* **2018**, *140*, 6249−6259.

(24) Green, M. P.; Hanson, K. J.; Carr, R.; Lindau, I. STM Observations of the Underpotential Deposition and Stripping of Pb on Au(111) under Potential Sweep Conditions. *J. Electrochem. Soc.* **1990**, *137*, 3493−3498.

(25) Gokcen, D.; Bae, S.-E.; Brankovic, S. R. Reaction Kinetics of Metal Deposition via Surface Limited Red-Ox Replacement of Underpotentially Deposited Metal Monolayers. *Electrochim. Acta* **2011**, *56*, 5545−5553.

(26) Fayette, M.; Liu, Y.; Bertrand, D.; Nutariya, J.; Vasiljevic, N.; Dimitrov, N. From Au to Pt via Surface Limited Redox Replacement of Pb UPD in One-Cell Configuration. *Langmuir* **2011**, *27*, 5650−5658.

(27) Toney, M. F.; Gordon, J. G.; Samant, M. G.; Borges, G. L.; Melroy, O. R.; Yee, D.; Sorensen, L. B. In-Situ Atomic Structure of Underpotentially Deposited Monolayers of Pb and Tl on Au(111) and Ag(111): A Surface X-Ray Scattering Study. *J. Phys. Chem.* **1995**, *99*, 4733−4744.

(28) Price, S. W. T.; Speed, J. D.; Kannan, P.; Russell, A. E. Exploring the First Steps in Core-Shell Electrocatalyst Preparation: In Situ Characterization of the Underpotential Deposition of Cu on Supported Au Nanoparticles. *J. Am. Chem. Soc.* **2011**, *133*, 19448−19458.

(29) Carino, E. V.; Kim, H. Y.; Henkelman, G.; Crooks, R. M. Site-Selective Cu Deposition on Pt Dendrimer-Encapsulated Nanoparticles: Correlation of Theory and Experiment. *J. Am. Chem. Soc.* **2012**, *134*, 4153−4162.

(30) Carino, E. V.; Crooks, R. M. Characterization of Pt@Cu Core@Shell Dendrimer-Encapsulated Nanoparticles Synthesized by Cu Underpotential Deposition. *Langmuir* **2011**, *27*, 4227−4235.

(31) Oviedo, O. A.; Velez, P.; Macagno, V. A.; Leiva, E. P. M. Underpotential Deposition: From Planar Surfaces to Nanoparticles. *Surf. Sci.* **2015**, *631*, 23−24.

(32) Oviedo, O. A.; Mariscal, M. M.; Leiva, E. P. M. Theoretical Studies of Preparation of Core-Shell Nanoparticles by Electrochemical Metal Deposition. *Electrochim. Acta* **2010**, *55*, 8244−8251.

(33) Romero-Romo, M.; Aldana-Gonzalez, J.; Botello, L. E.; Montes de Oca, M. G.; Ramirez-Silva, M. T.; Corona-Avendano, S.; Palomar-Pardave, M. Electrochemical Nucleation and Growth of Cu onto Au Nanoparticles Supported on a Si(111) Wafer Electrode. *J. Electroanal. Chem.* **2017**, *791*, 1−7.

(34) Kumar, A.; Buttry, D. A. Size-Dependent Underpotential Deposition of Copper on Palladium Nanoparticles. *J. Phys. Chem. C* **2015**, *119*, 16927−16933.

(35) Zhu, S.; Yue, J.; Qin, X.; Wei, Z.; Liang, Z.; Adzic, R. R.; Brankovic, S. R.; Du, Z.; Shao, M. The Role of Citric Acid in Perfecting Platinum Monolayer on Palladium Nanoparticles during the Surface Limited Redox Replacement Reaction. *J. Electrochem. Soc.* **2016**, *163*, D3040−D3046.

(36) Scott, R. W. J.; Wilson, O. M.; Crooks, R. M. Synthesis, Characterization, and Applications of Dendrimer-Encapsulated Nanoparticles. *J. Phys. Chem. B* **2005**, *109*, 692−704.

(37) Yeung, L. K.; Lee, C. T.; Johnston, K. P.; Crooks, R. M. Catalysis in Supercritical CO2 Using Dendrimer-Encapsulated Palladium Nanoparticles. *Chem. Commun.* **2001**, 2290−2291.

(38) Zhao, M.; Sun, L.; Crooks, R. M. Preparation of Cu Nanoclusters within Dendrimer Templates. *J. Am. Chem. Soc.* **1998**, *120*, 4877−4878.

(39) Ye, R.; Zhukhovitskiy, A. V.; Deraedt, C. V.; Toste, F. D.; Somorjai, G. A. Supported Dendrimer-Encapsulated Metal Clusters: Toward Heterogenizing Homogeneous Catalysts. *Acc. Chem. Res.* **2017**, *50*, 1894−1901.

(40) Astruc, D.; Wang, D.; Deraedt, C.; Liang, L.; Ciganda, R.; Ruiz, J. Catalysis Inside Dendrimers. *Synthesis* **2015**, *47*, 2017−2031.

(41) Bronstein, L. M.; Shifrina, Z. B. Dendrimers as Encapsulating, Stabilizing, or Directing Agents for Inorganic Nanoparticles. *Chem. Rev.* **2011**, *111*, 5301−5344.

(42) Luo, L.; Zhang, L.; Henkelman, G.; Crooks, R. M. Unusual Activity Trend for CO Oxidation on PdxAu140-X@Pt Core@Shell Nanoparticle Electrocatalysts. *J. Phys. Chem. Lett.* **2015**, *6*, 2562−2568.

(43) Luo, L.; Zhang, L.; Duan, Z.; Lapp, A. S.; Henkelman, G.; Crooks, R. M. Efficient CO Oxidation Using Dendrimer-Encapsulated Pt Nanoparticles Activated with < 2% Cu Surface Atoms. *ACS Nano* **2016**, *10*, 8760−8769.

(44) Luo, L.; Duan, Z.; Li, H.; Kim, J.; Henkelman, G.; Crooks, R. M. Tunability of the Adsorbate Binding on Bimetallic Alloy Nanoparticles for the Optimization of Catalytic Hydrogenation. *J. Am. Chem. Soc.* **2017**, *139*, 5538−5546.

(45) Neurock, M.; Janik, M.; Wieckowski, A. A First Principles Comparison of the Mechanism and Site Requirements for the Electrocatalytic Oxidation of Methanol and Formic Acid over Pt. *Faraday Discuss.* **2009**, *140*, 363.

(46) Duchesne, P. N.; Li, Z. Y.; Deming, C. P.; Fung, V.; Zhao, X.; Yuan, J.; Regier, T.; Aldalbahi, A.; Almarhoon, Z.; Chen, S.; Jiang, D.; Zheng, N.; Zhang, P. Golden Single-Atomic-Site Platinum Electrocatalysts. *Nat. Mater.* **2018**, *17*, 1033−1039.

(47) Rodriguez, P.; Garcia-Araez, N.; Koverga, A.; Frank, S.; Koper, M. T. M. CO Electroxidation on Gold in Alkaline Media: A Combined Electrochemical, Spectroscopic, and DFT Study. *Langmuir* **2010**, *26*, 12425−12432.

(48) Yancey, D. F.; Chill, S. T.; Zhang, L.; Frenkel, A. I.; Henkelman, G.; Crooks, R. M. A Theoretical and Experimental Examination of Systematic Ligand-Induced Disorder in Au Dendrimer-Encapsulated Nanoparticles. *Chem. Sci.* **2013**, *4*, 2912−2921.

(49) Kresse, G.; Hafner, J. Ab Initio Molecular Dynamics for Liquid Metals. *Phys. Rev. B: Condens. Matter Mater. Phys.* **1993**, *47*, 558−561.

(50) Kresse, G.; Furthmuller, J. Efficiency of Ab-Initio Total Energy Calculations for Metals and Semiconductors Using a Plane-Wave Basis Set. *Comput. Mater. Sci.* **1996**, *6*, 15−50.

(51) Blochl, P. E. Projector Augmented-Wave Method. *Phys. Rev. B: Condens. Matter Mater. Phys.* **1994**, *50*, 17953.

(52) Kresse, G.; Joubert, D. From Ultrasoft Pseudopotentials to the Projector Augmented-Wave Method. *Phys. Rev. B: Condens. Matter Mater. Phys.* **1999**, *59*, 1758−1775.

(53) Perdew, J. P.; Ruzsinszky, A.; Csonka, G. I.; Vydrov, O. A.; Scuseria, G. E.; Constantin, L. A.; Zhou, X.; Burke, K. Restoring the Density-Gradient Expansion for Exchange in Solids and Surfaces. *Phys. Rev. Lett.* **2008**, *100*, 136406.

(54) Taylor, C. D.; Wasileski, S. A.; Filhol, J.-S.; Neurock, M. First Principles Reaction Modeling of the Electrochemical Interface: Consideration and Calculation of a Tunable Surface Potential from Atomic and Electronic Structure. *Phys. Rev. B: Condens. Matter Mater. Phys.* **2006**, *73*, 165402.

(55) Mathew, K.; Sundararaman, R.; Letchworth-Weaver, K.; Arias, T. A.; Hennig, R. G. Implicit Solvation Model for Density-Functional Study of Nanocrystal Surfaces and Reaction Pathways. *J. Chem. Phys.* **2014**, *140*, No. 084106.

(56) Duan, Z.; Henkelman, G. Calculations of the PH-Dependent Onset Potential for CO Electro-Oxidation on Au(111). *Langmuir* **2018**, *34*, 15268−15275.

(57) Duan, Z.; Henkelman, G. Theoretical Resolution of the Exceptional Oxygen Reduction Activity of Au(100) in Alkaline Media. *ACS Catal.* **2019**, *9*, 5567−5573.

(58) Karlberg, G. S.; Jaramillo, T. F.; Skulason, E.; Rossmeisl, J.; Bligaard, T.; Norskov, J. K. Cyclic Voltammograms for H on Pt(111) and Pt(100) from First Principles. *Phys. Rev. Lett.* **2007**, *99*, 126101.

(59) Weitzner, S. E.; Dabo, I. Quantum-Continuum Simulation of Underpotential Deposition at Electrified Metal-Solution Interfaces. *npj Comput. Mater.* **2017**, *3*, 1.

(60) Trasatti, S.; Petrii, O. A. Real Surface Area Measurements in Electrochemistry. *Pure Appl. Chem.* **1991**, *63*, 711−734.

(61) Hernández, J.; Solla-Gullón, J.; Herrero, E. Gold Nanoparticles Synthesized in a Water-in-Oil Microemulsion: Electrochemical Characterization and Effect of the Surface Structure on the Oxygen Reduction Reaction. *J. Electroanal. Chem.* **2004**, *574*, 185−196.

(62) Hernandez, J.; Solla-Gullon, J.; Herrero, E.; Aldaz, A.; Feliu, J. M. Characterization of the Surface Structure of Gold Nanoparticles and Nanorods Using Structure Sensitive Reactions. *J. Phys. Chem. B* **2005**, *109*, 12651−12654.

(63) Hebie, S.; Kokoh, K. B.; Servat, K.; Napporn, T. W. Shape-Dependent Electrocatalytic Activity of Free Gold Nanoparticles toward Glucose Oxidation. *Gold Bull.* **2013**, *46*, 311−318.

(64) Jeyabharathi, C.; Zander, M.; Scholz, F. Underpotential Deposition of Lead on Quasi-Spherical and Faceted Gold Nanoparticles. *J. Electroanal. Chem.* **2018**, *819*, 159−162.

(65) Velez, P.; Cuesta, A.; Leiva, E. P. M.; Macagno, V. A. The Underpotential Deposition That Should Not Be: Cu(1 × 1) on Au(111). *Electrochem. Commun.* **2012**, *25*, 54−57.

(66) Sanchez, C.; Leiva, E. P. M. Cu Underpotential Deposition on Au(111) and Au(100). Can This Be Explained in Terms of the Energetics of the Cu/Au System? *Electrochim. Acta* **1999**, *45*, 691−697.

(67) Borges, G. L.; Kanazawa, K. K.; Gordon, J. G. An In-Situ Electrochemical Quartz Crystal Microbalance Study of the Underpotential Deposition of Copper on Au(111) Electrodes. *J. Electroanal. Chem.* **1994**, *364*, 281−284.

(68) Futamata, M. Coadsorption of Anions and Water Molecule during Underpotential Deposition of Cu and Pb on the Au (1 1 1) Electrode Surface. *Chem. Phys. Lett.* **2001**, *333*, 337−343.